Ultra-compact and efficient standing-wave electro-optic modulator in lithium niobate

Citation for the original published paper (version of record):
Gao, Y., Sun, Y., Andrekson, P. et al (2026). Ultra-compact and efficient standing-wave electro-optic modulator in lithium niobate. Optica, 13(7): 1254-1260. http://dx.doi.org/10.1364/OPTICA.600213

(article starts on next page)

OPTICA

Ultra-compact and efficient standing-wave electro-optic modulator in lithium niobate

YAN GAO, YI SUN, PETER ANDREKSON, AND JOCHEN SCHRÖDER*

Department of Microtechnology and Nanoscience (MC2), Chalmers University of Technology, Göteborg, Sweden
*Jochen.schroeder@chalmers.se

Received 1 April 2026; revised 28 May 2026; accepted 9 June 2026; published 2 July 2026

Electro-optic (EO) modulators are fundamental building blocks in photonic systems, with broad applications in optical communications, computing, sensing, and quantum information processing. Thin-film lithium niobate (LN) has emerged as a leading platform for EO modulators owing to its strong Pockels effect and its potential for low-power, scalable, and cost-effective integrated photonic systems. To achieve low driving voltage at high modulation speeds, traveling wave (TW) electrodes are widely employed to extend the interaction length. However, the voltage-length product of TW LN modulators remains intrinsically limited and cannot be straightforwardly enhanced, resulting in device footprints on the order of several centimeters. To overcome this limitation, we propose a high-*Q* micro-structured standing-wave (SW) electrode design that significantly enhances intrinsic modulation efficiency, and as a result, can drastically reduce the electrode length. We experimentally demonstrate a single-drive SW LN phase modulator with a voltage-length product of $V_\pi \cdot L = 1\,\mathrm{V} \cdot \mathrm{cm}$ (corresponding to $0.5\,\mathrm{V} \cdot \mathrm{cm}$ in a push-pull configuration) using a total electrode length of only 1 mm. Our device exhibits a 5.6-fold improvement in intrinsic modulation efficiency and a 20-fold reduction in footprint compared with a typical TW modulator. In addition to its compactness and high efficiency, the proposed SW modulator, to our knowledge, offers several unique advantages, including impedance-loading-free operation, relaxed velocity-matching requirements, and high reciprocity. These attributes make the SW modulator a promising building block for ultra-efficient and densely integrated EO circuits, such as EO frequency combs, optical switches, and microwave-photonics systems.

https://doi.org/10.1364/OPTICA.600213

1. INTRODUCTION

Electro-optic (EO) modulator is a key workhorse for converting electrical signals into optical signals and plays a central role in optical communications, microwave photonics, frequency metrology, and a wide range of EO systems to convert electrical signals into optical signals [1–6]. Various physical mechanisms have been exploited to realize EO modulation, including carrier plasma dispersion [3], electro-absorption [7], and the linear Pockels effect [8].

EO modulators implemented in photonic integrated circuits [9] (PICs) have attracted significant research interest due to their potential for integration, miniaturization, and large-scale manufacturing. Over the past decades, multiple material platforms have been investigated, including silicon (Si) [10], indium phosphide (InP) [11], aluminum nitride (AlN) [12], gallium arsenide (GaAs) [13], silicon nitride (SiN_x) [14], lithium niobate (LN) [15], and lithium tantalate [16]. Among these platforms, LN stands out owing to its large Pockels coefficient ($r_{33} = 30.9$ pm/V) and its unique capability to simultaneously support electro-optic (EO), nonlinear and acousto-optic effects, together with a relatively large refractive index and broad optical transparency window [17–20].

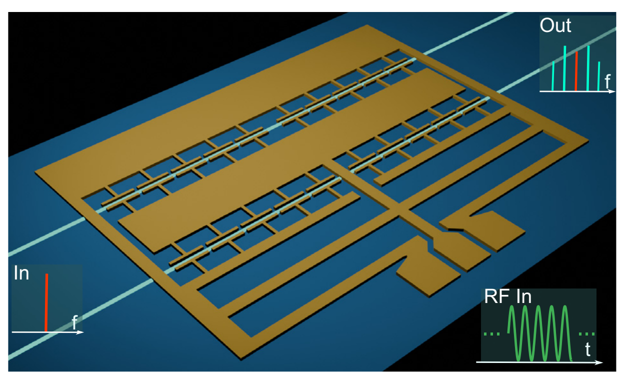

Fig. 1. Schematic of the standing-wave modulator.

To meet the rapidly increasing demands for circuit complexity in applications such as data center interconnects [21] and optical computing [22], substantial efforts have been devoted to improving the intrinsic modulation efficiency, which represents the modulation efficiency per unit length and can be indicated by the well-known voltage-length product ($V_\pi \cdot L$). A classical approach employs traveling-wave (TW) electrodes, which enable low drive voltage and high-speed operation by extending the RF–optical interaction length [15,23–26]. However, such distributed electrode configurations typically require centimeter-scale active lengths to achieve a low drive voltage, posing a major challenge for dense, circuit-level integration. This limitation becomes particularly restrictive for applications such as EO frequency combs [27], digital-to-analog converters (DACs) [28], and microwave-photonic engines [29]. Recent studies have shown that the DC intrinsic modulation efficiency of TW LN modulators cannot be straightforwardly improved due to an inherent trade-off between optical insertion loss (IL) and the voltage-length product $V_\pi \cdot L$, arising from optical-to-plasmonic mode coupling in metal electrodes [30]. To overcome this limitation, alternative electrode and cladding engineering approaches have been explored. For example, replacing absorptive metallic electrodes with transparent conductive oxides such as indium tin oxide (ITO) has enabled a significantly reduced DC $V_\pi \cdot L$ of $1.02\ \mathrm{V \cdot cm}$ in a push-pull configuration [31]. However, the use of ITO increases fabrication complexity and introduces additional optical loss due to its limited transparency. Similarly, employing high-permittivity claddings can enhance the external electric field in the waveguide core and improve intrinsic modulation efficiency (with a reported $V_\pi \cdot L$ of $1.34\ \mathrm{V \cdot cm}$) [32], but at the cost of increased optical loss and material integration complexity. Approaches based on slow-light effects [33,34] or optical resonators [35,36] can achieve efficient and compact modulators; however, their practical deployment is often limited by narrow optical bandwidths and high sensitivity to environmental perturbations.

In this work, we address these challenges by introducing a high-Q, micro-structured standing-wave (SW) electrode architecture (see Fig. 1) that significantly enhances the effective RF power and, consequently, improves the intrinsic modulation efficiency [37–39]. Due to the low-loss micro-structured electrodes [24], we successfully demonstrate a high Q_0 (26) microwave resonator. As a result, we experimentally demonstrate a single-drive SW LN phase modulator with a $V_\pi \cdot L^{@14\,\mathrm{GHz}} = 1\ \mathrm{V \cdot cm}$, corresponding to $0.5\ \mathrm{V \cdot cm}$ in a push-pull configuration, while using a total electrode length of only around 1 mm. Compared to a representative TW LN modulator [15], which exhibits $V_\pi \cdot L^{\mathrm{DC}} = 2.8\ \mathrm{V \cdot cm}$ and an electrode length of 20 mm, our device achieves a 5.6-fold improvement in $V_\pi \cdot L$ and a 20-fold reduction in footprint. Beyond its high efficiency and compactness, the proposed SW modulator offers several additional advantages, including impedance-loading-free operation, relaxed phase-matching requirements, and high reciprocity. Even at the expense of a very narrow EO bandwidth (0.53 GHz), these features make the efficient SW modulator particularly attractive for applications that do not require a very broad EO bandwidth, such as compact and flat EO combs, high-speed integrated EO switches, efficient microwave-photonics systems, microwave-to-photons/phonon transducers, and quantum photonic computing. Moreover, the proposed SW electrode concept is general and can be extended to other EO material platforms to enhance their modulation performance.

2. LOW-LOSS SEGMENTED RF ELECTRODE

Achieving efficient SW modulators requires the use of a high-Q RF resonator, which can be realized by minimizing RF waveguide losses. However, in standard thin-film LN modulators, RF propagation losses are typically high ($0.7\ \mathrm{dB \cdot cm^{-1} \cdot GHz^{-1/2}}$), primarily due to significant ohmic losses caused by the current crowding effect [24] in closely spaced metallic electrodes. To mitigate this issue, we employ segmented electrodes [24,40] to construct the RF resonator, effectively suppressing current crowding. The segmented electrode is formed by periodically loading T-sections onto a uniform coplanar waveguide (CPW), as shown in Fig. 2.

Figure 3 shows the calculated RF propagation loss and effective index of the segmented electrode. The calculation method can be found in Supplement 1. The total RF loss originates from two contributions: losses in the original uniform CPW and losses associated with the T-sections. Here, we present the optimization results with respect to two key design parameters: the signal pad width W_S and the T-section extruding length b. As shown in Fig. 3(a), the RF loss strongly depends on both parameters. Increasing W_S leads to a monotonic reduction in RF loss due to decreased ohmic resistance, similar to the trend in a uniform CPW transmission line. In contrast, as b increases, the RF loss initially decreases and then increases after reaching a minimum. This behavior arises from competing effects: increasing b reduces the ohmic loss of the uniform line while simultaneously increasing losses in the T-sections due to changes in the shunt admittance Y_a.

After optimization, the calculated RF loss can be reduced to as low as $0.1\ \mathrm{dB \cdot cm^{-1} \cdot GHz^{-1/2}}$, which is significantly smaller than the previously reported result of $0.26\ \mathrm{dB \cdot cm^{-1} \cdot GHz^{-1/2}}$ [24]. The RF effective index ranges from 3–5, depending on the design parameters, and is substantially higher than the optical effective index (around 2.2) due to the slow-wave effect in segmented electrodes [40]. In TW modulators, this large RF effective index imposes stringent phase-matching requirements, often necessitating special substrates such as low-permittivity quartz [24] or undercut silicon [41]. In contrast, for the SW modulator considered here, the ultra-short electrode length allows phase mismatch to be neglected, enabling operation on a standard silicon substrate without any special substrate engineering.

3. HIGH-Q SW MODULATOR

The low-loss segmented electrodes enable the construction of a high-Q RF resonator, as shown in Fig. 4(a). This RF resonator operates as a Fabry–Pérot (FP)-like cavity, where the RF wave reflects back and forth between two reflective mirrors [37] (open-ended transmission line), as illustrated in Fig. 4(b). The equivalent transmission line model for the RF resonator is shown in Fig. 4(c). In this model, line a represents the active modulation electrode; line b is the stub tuning network for impedance matching between the source and resonator, and line c is the power feeding line.

Similar to a TW modulator, the total phase change in the active region of a SW modulator can be calculated by integrating the local phase change of the photon along its propagation path:

$$\Phi(\omega) = \frac{\pi}{V_\pi \cdot L} \int_{-L}^{0} V(z) \mathrm{d}z, \tag{1}$$

where $V_\pi \cdot L$ is the voltage-length product in the corresponding non-resonant modulator, and $V(z)$ is the distributed voltage in the active region. For an arbitrary transmission line circuit, the voltage $V(z)$ can be calculated using the ABCD matrix method, with the appropriate boundary conditions at the source and load [42].

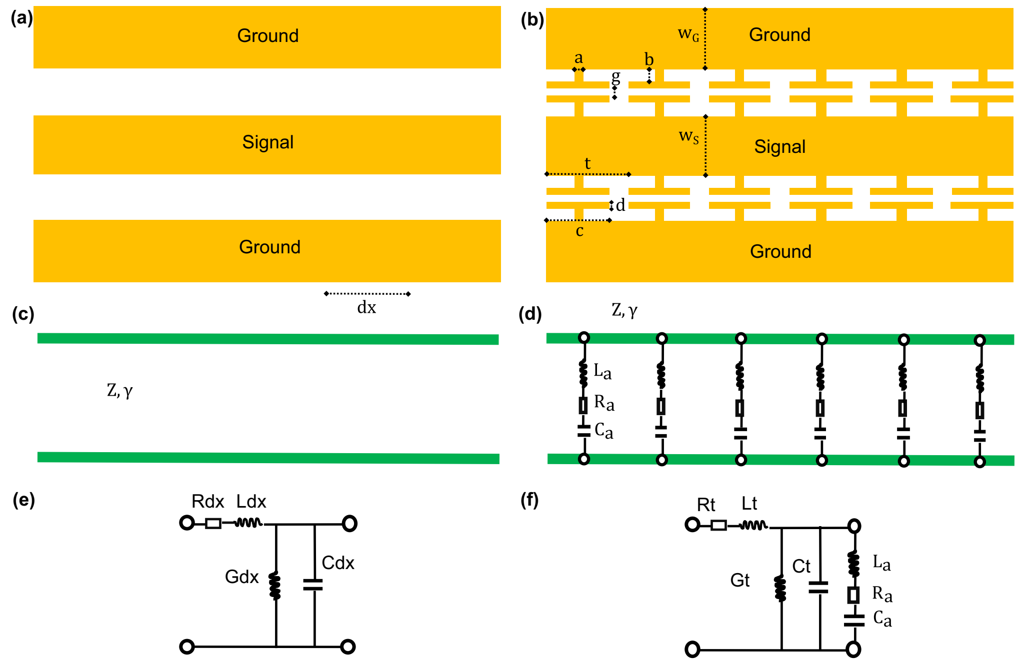

Fig. 2. Schematic diagram of (a) a uniform electrode and (b) a periodic segmented electrode; (c), (d) the corresponding transmission line model; and (e), (f) the corresponding equivalent circuit.

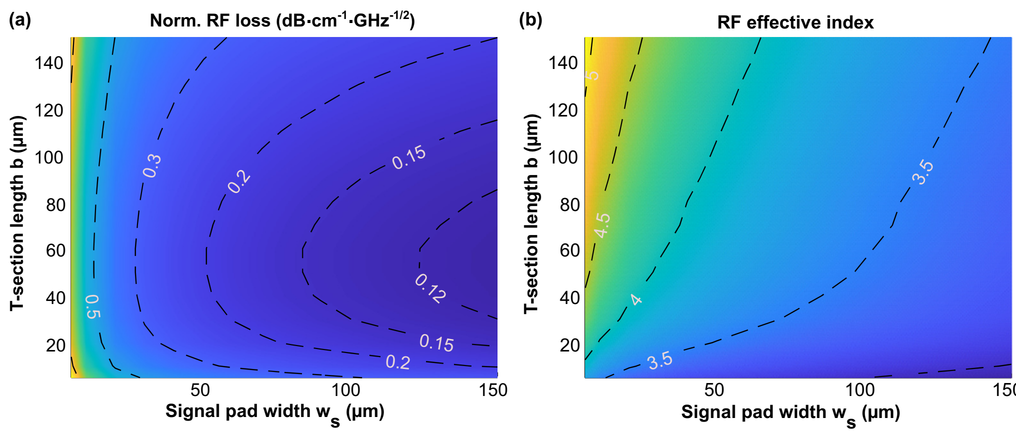

Fig. 3. Optimization result for (a) the normalized RF propagation losses and (b) RF effective index of the segmented electrodes. W_S and b indicate the center signal pad width and the extruded length of T-section, and the definition can be found in Fig. 2(b).

Figure 5 presents the optimization results for the SW modulator. The impedance of the SW modulator (considering only the active region: line a) is typically much smaller than 50 Ω, and a phase matching (line b) is needed to achieve the impedance matching. According to transmission line theory, the tuning stub length L_b is crucial for achieving the perfect matching condition. As shown in Fig. 5(a), the input impedance Z_{in}, looking from the source, and the S_{11} parameter, change dramatically with variations in L_b. Once the impedance is properly matched, the S_{11} parameter becomes less than −25 dB. Notably, for the matched case, the entire resonator (including the matching network) is constructed as a single-port network with a 50 Ω impedance, meaning no additional load impedance is required, simplifying the overall circuit design.

Due to resonance enhancement, the intracavity voltage is significantly higher than the source voltage ($V_s = 1$ V in the simulation), as shown in Fig. 5(c). Since the RF resonator is symmetric along the power feeding line b, we show only the voltage distribution along the left arm. Owing to the SW nature and the symmetry of the voltage distribution, the modulation indices for the waveguide with bi-directional inputs are identical, resulting in high reciprocity. In contrast, there is a non-reciprocal modulation response for the TW modulator. The enhanced intracavity power can significantly reduce the $V_\pi \cdot L$ (for single-arm phase modulator without push-pull configuration), as shown in Fig. 5(d). As discussed in Section 2, the RF loss in the active region (line a) can be reduced to approximately 0.1 $\text{dB} \cdot \text{cm}^{-1} \cdot \text{GHz}^{-1/2}$ by using segmented electrodes. However, in the RF resonator, the effective loss α is determined by the losses in lines a, b, and c, which together contribute a higher effective loss than that in line a alone. As shown in Fig. 5(e), the value of V_π for the SW modulator is strongly dependent on the effective loss inside the RF resonator. Assuming $\alpha = 0.1 \cdot \text{cm}^{-1} \cdot \text{GHz}^{-1/2}$, the V_π can be as low as approximately

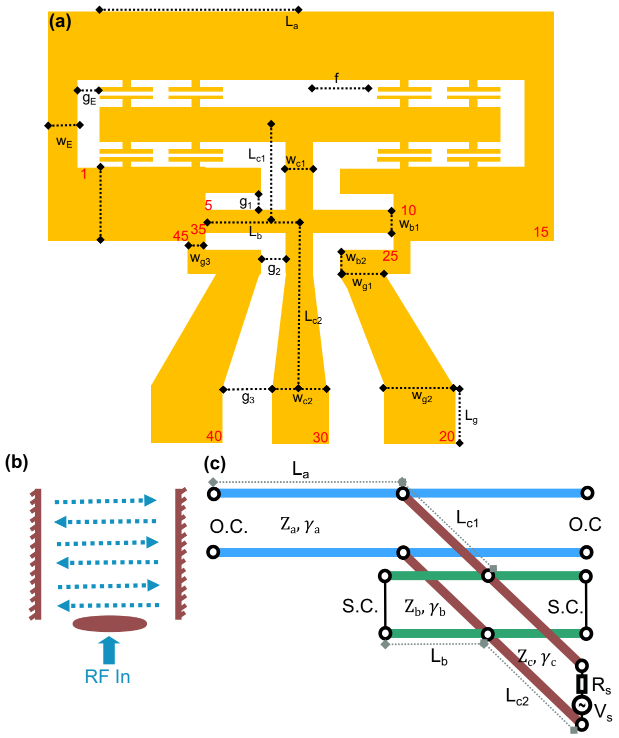

Fig. 4. (a) Layout and the geometric parameters of the SW modulator; the red number is used to help identify the electrode node position. (b) Conceptual diagram of the RF resonator; and (c) the equivalent transmission line circuit.

6 V, representing a 16 dB enhancement compared with the value in a TW modulator, as shown [Fig. 5(f)].

4. DEVICE FABRICATION AND MODULATOR CHARACTERIZATION

The device is fabricated on a centimeter-scale chip diced from a commercial 4 inch LN wafer (NanoLN). The optical waveguide is first fabricated using E-beam lithography and ion^{+} beam etching, following a similar process reported in our previous work [43,44]. The E-beam resist ma-N 2405 with a thickness of approximately 800 nm is used to define the optical waveguide. Sputtered Si_3N_4 of around 4 nm is used to promote the adhesion between resist and LN. Next, 400 nm PECVD SiO_2 is deposited and patterned via photonlithography and wet etching to create an isolation layer between the optical waveguide and metallic electrodes. Finally, 1 μm thick gold electrodes are deposited via vacuum evaporation and then patterned via photon lithography and a bi-layer lift-off process (LOR10B/S1813).

The fabricated device is shown in Fig. 6(a), with the full SW modulator having a total active length of only 1 mm. The zoomed-in image in Fig. 6(a) provides a detailed view of the segmented T-sections and the optical waveguide that passes through the electrodes, with a SiO_2 protection window in between. To characterize the RF spectrum response of the SW modulator, we measure the device S-parameters using a vector network analyzer (VNA). Figure 6(c) shows a measured optical spectrum at RF power of 34 dBm, in which 17 comb lines and an approximately 1.8 nm bandwidth can be obtained within only one single-phase modulator. A typical measured S_{11} parameter is shown in Fig. 6(d). By fitting the response curve with a Lorentzian function, the resonant frequency f_0 (13.74 GHz) and quality factor (Q-factor) of the RF resonator (26) are obtained. This high Q value corresponds to an estimated equivalent RF loss of approximately $0.3\,\mathrm{dB}\cdot\mathrm{cm}^{-1}\cdot\mathrm{GHz}^{-1/2}$, which is much smaller than that in the conventional uniform electrodes with a loss of around $0.7\,\mathrm{dB}\cdot\mathrm{cm}^{-1}\cdot\mathrm{GHz}^{-1/2}$ [24]. The equivalent RF loss represents the average value between the segmented RF electrodes [line a in Fig. 4(c)] and the uniform RF electrodes [line b and c in Fig. 4(c)]. Considering the RF loss in line b and c is much larger than that in lines a from the calculation, the actual loss in segmented electrodes should be even smaller than the measured value. Furthermore, the EO 3 dB bandwidth can be estimated from S_{11}, which is 0.53 GHz. Even with the scarification of the EO bandwidth, the high-Q SW modulator shows great potential to achieve high modulation efficiency.

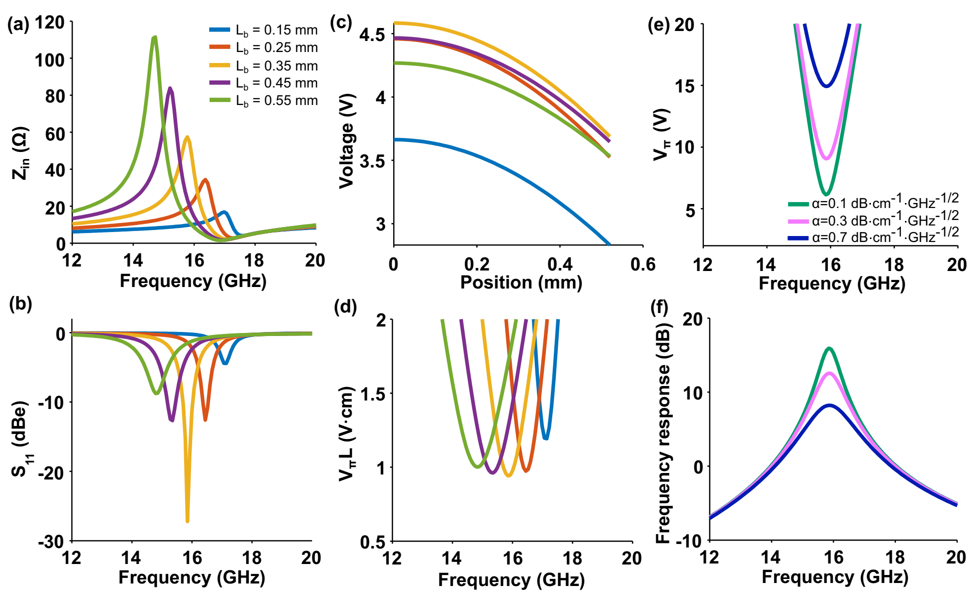

Fig. 5. (a) Simulated impedance, (b) S_{11}, (c) intra-cavity voltage, and (d) voltage-length product for the SW modulator with different tuning stub lengths, and the effective RF losses are set to be $\alpha = 0.3\,\mathrm{dB}\cdot\mathrm{cm}^{-1}\cdot\mathrm{GHz}^{-1/2}$. (e) Simulated V_π and (f) frequency response of the modulator with different RF propagation losses.

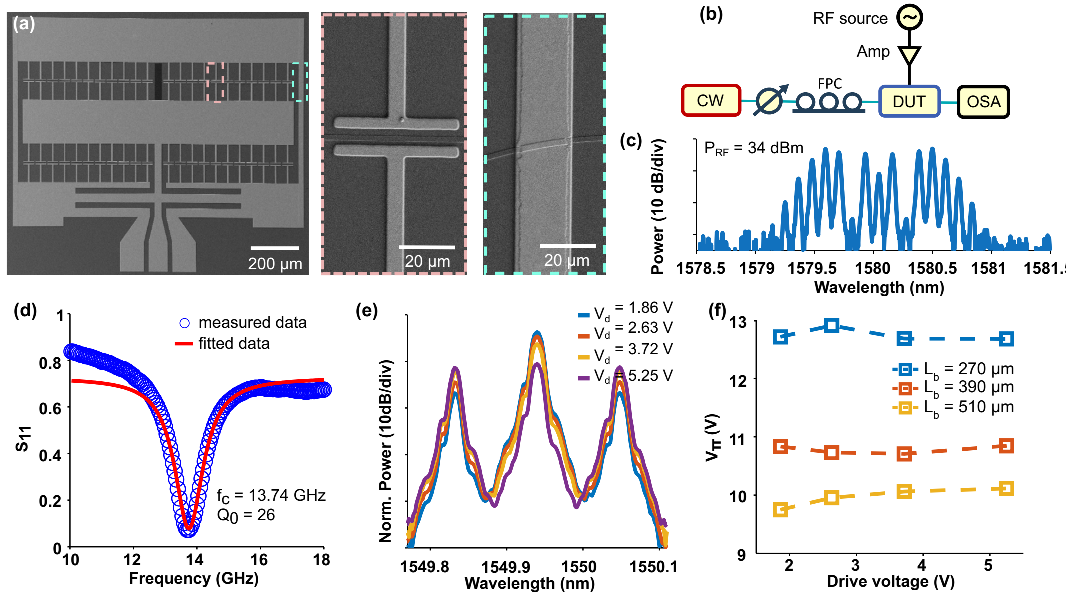

Fig. 6. (a) SEM figures of the SW modulator. (b) Setup of the high frequency V_π measurements. (c) Measured optical spectrum at RF power of 34 dBm. (d) S_{11} measurement result of the SW electrode. (e) Measured optical spectrum of the SW phase modulator with different drive voltages. (f) Measured V_π for devices with different L_b.

Table 1. Summary of Efficient EO Modulators in LN

Type	L (mm)	V_π^{PM} (V)[a]	$V_\pi \cdot L^{PM}$ (V · cm)[a]	IL (dB)	3 dB EO BW (GHz)	Optical BW (nm)	Year
Standard TW	20	2.8	5.6	<0.5	40	NL[b]	2018 [15]
Folded TW	75	0.52	3.9	8	2.5	NL	2025 [26]
Transparent electrodes	5	4.08	2.04	2.9	108	NL	2025 [31]
High-K material caldding	4	7.05	2.82	0.5	>67	NL	2023 [32]
Slow light waveguide	2.8	8.8	2.46	1.68	>67	6	2025 [33]
	1	4.2	0.42	12.5	>110	4.4[c]	2025 [34]
SW electrodes	1	10@14 GHz	1@14 GHz	0.9	0.53	NL	This work

[a]Indicates the corresponding values in a single-phase modulator, and the value corresponds to twice, as the value in a push-pull configuration in an intensity modulator. The value indicates a DC half-wave voltage unless there is specification.
[b]Typically there is no limitation of the optical BW.
[c]This indicates the maximum usable slow-light region, where $V_\pi \cdot L$ and IL vary significantly with different wavelengths.

Since there is no DC modulation response in the SW modulator, we directly measure the high-frequency V_π by evaluating the modulation index through a sideband measurement method [45]. The measurement setup is shown in Fig. 6(b), where an RF signal at the RF resonant frequency is used to drive the modulator, and the output spectrum is recorded using an optical spectrum analyzer. The modulation of the optical carrier results in energy transfer from the optical carrier to its sidebands, where the optical power of the carrier signal and the sidebands are related by the Jacobi–Anger identity. For small signal modulation, the modulation index η can be derived by evaluating the ratio of the zero-order and the first-order Bessel functions of the first kind, $\Delta P = P_1/P_0 = J_1^2(\eta)/J_0^2(\eta)$, where P_0 and P_1 represent the optical power for the carrier and first sideband, respectively. Once the modulation index is determined, the modulator V_π at high frequency can be expressed as: $V_\pi^f = V_d/\eta \cdot \pi$, where V_d is the drive voltage. A very detailed discussion about the sideband measurement method can be found in [46].

The optical spectrum measured under different drive voltages of the device is shown in Fig. 6(e). As the RF drive voltage increases, more optical power is transferred to the sidebands. The extracted V_π at the resonance frequency is shown in Fig. 6(f). With a proper tuning stub length ($L_b = 510$ μm), the V_π for a single-phase modulator is measured to be approximately 10 V (equivalent to $V_\pi = 5$ V in a push-pull configuration), corresponding to a $V_\pi \cdot L = 1$ V · cm (equivalent to $V_\pi \cdot L = 0.5$ V · cm in a push-pull configuration). The measurement result aligns well with the simulation results for a similar RF loss [see Fig. 5(e)]. Moreover, the SW modulator also features a small insertion loss of <0.9 dB and the facet coupling loss is estimated to be 6 dB/facet. Table 1 summarizes the state-of-the-art results of different types of efficient EO modulators in LN. Compared to these results, our SW modulator stands out due to its ultra-small footprint, high intrinsic modulation efficiency, ultra-low insertion loss, and very large optical BW, making it highly attractive for complex on-chip EO circuits. Furthermore, we test the power-handling capability of our SW modulator, and no device damage is observed even with an RF input power of 39 dBm. For operation at higher RF power, further consideration of thermal sinking is required to maintain proper fiber–chip coupling and reliable RF probe contact.

5. CONCLUSION

In conclusion, we experimentally demonstrate a high-Q RF resonator using low-loss segmented electrodes. Leveraging the strong cavity-enhancement effect provided by the RF resonator, we successfully demonstrate an ultra-compact (1 mm) single-drive LN EO phase modulator with high intrinsic modulation efficiency, achieving a $V_\pi \cdot L^{@14\,\mathrm{GHz}} = 1\ \mathrm{V \cdot cm}$ (or $0.5\ \mathrm{V \cdot cm}$ in a push-pull configuration). Thanks to the ultra-compact device size and the straightforward optical design (a bare optical waveguide), our device exhibits both low insertion loss and a large optical bandwidth (BW). In addition to these key performance metrics, our SW modulator offers several unique advantages derived from the innovative resonant circuit design. These advantages include: impedance-loading-free operation, relaxed phase-matching requirements, and high reciprocity. With these unique properties, we believe the SW modulator opens new possibilities for applications in high-speed integrated EO switches, compact and flat EO combs, efficient microwave-photonic systems, and quantum-optic computations.

While the SW design significantly enhances intrinsic modulation efficiency, the measured V_π is still limited to 10 V, which remains relatively high considering the growing demand for low energy consumption in modern EO systems. This relatively large V_π is mainly caused by the short modulator active length (1 mm), which results from operating in the fundamental RF mode. In principle, we can use a higher-order longitudinal mode to achieve a much longer modulation active length, thereby significantly reducing the actual V_π. However, the challenges associated with a higher-order RF mode need to be further addressed: (1) the cavity-enhancement factor will decrease, and (2) the longer electrode will significantly raise the phase-matching requirement. Another way to reduce V_π is to operate at a much lower RF frequency, which will naturally increase the RF cavity length and thus significantly reduce V_π. Moreover, lower V_π can also be achieved by combining the SW electrodes with other optical or substrate engineering approaches, such as recycling the optical passes or those listed in Table 1, due to the high compatibility of our device with existing designs. Overall, we are optimistic about the potential of our SW modulators and believe they will become a key building block for ultra-efficient and densely integrated on-chip EO circuits in the future.

Funding. Swedish Research Council (VR-2017-05157, VR-2021-04241, VR-2016-06077).

Acknowledgment. The authors thank the cleanroom staff from Myfab at Chalmers Nanofabrication Laboratory for discussion and training and thank Prof. Victor Torres-Company for valuable discussions and insightful suggestions.

Disclosures. The authors declare no conflicts of interest.

Data availability. Data underlying the results presented in this paper are available in Ref. [47].

Supplemental document. See Supplement 1 for supporting content.

REFERENCES

1. A. Boes, L. Chang, C. Langrock, *et al.*, "Lithium niobate photonics: unlocking the electromagnetic spectrum," Science **379**, eabj4396 (2023).
2. E. L. Wooten, K. M. Kissa, A. Yi-Yan, *et al.*, "A review of lithium niobate modulators for fiber-optic communications systems," J. Sel. Top. Quantum Electron. **6**, 69–82 (2000).
3. G. T. Reed, G. Mashanovich, F. Y. Gardes, *et al.*, "Silicon optical modulators," Nat. Photonics **4**, 518–526 (2010).
4. J. Witzens, "High-speed silicon photonics modulators," Proc. IEEE **106**, 2158–2182 (2018).
5. M. Howerton, R. Moeller, A. Greenblatt, *et al.*, "Fully packaged, broadband $LiNbO_3$ modulator with low drive voltage," IEEE Photonics Technol. Lett. **12**, 792–794 (2000).
6. D. Marpaung, J. Yao, and J. Capmany, "Integrated microwave photonics," Nat. Photonics **13**, 80–90 (2019).
7. J. Liu, M. Beals, A. Pomerene, *et al.*, "Waveguide-integrated, ultralow-energy GeSi electro-absorption modulators," Nat. Photonics **2**, 433–437 (2008).
8. L. N. Binh, "Lithium niobate optical modulators: devices and applications," J. Cryst. Growth **288**, 180–187 (2006).
9. T. David, Z. Aaron, E. B.John, *et al.*, "Roadmap on silicon photonics," J. Opt. **18**, 073003 (2016).
10. Q. Xu, B. Schmidt, S. Pradhan, *et al.*, "Micrometre-scale silicon electro-optic modulator," Nature **435**, 325–327 (2005).
11. T. Liu, F. Pagliano, R. van Veldhoven, *et al.*, "Low-voltage MEMS optical phase modulators and switches on a indium phosphide membrane on silicon," Appl. Phys. Lett. **115**, 251104 (2019).
12. C. Xiong, W. H. Pernice, and H. X. Tang, "Low-loss, silicon integrated, aluminum nitride photonic circuits and their use for electro-optic signal processing," Nano Lett. **12**, 3562–3568 (2012).
13. D. Hall, A. Yariv, and E. Garmire, "Optical guiding and electro-optic modulation in GaAs epitaxial layers," Opt. Commun. **1**, 403–405 (1970).
14. K. Alexander, J. P. George, J. Verbist, *et al.*, "Nanophotonic pockels modulators on a silicon nitride platform," Nat. Commun. **9**, 3444 (2018).
15. C. Wang, M. Zhang, X. Chen, *et al.*, "Integrated lithium niobate electro-optic modulators operating at CMOS-compatible voltages," Nature **562**, 101–104 (2018).
16. C. Wang, Z. Li, J. Riemensberger, *et al.*, "Lithium tantalate photonic integrated circuits for volume manufacturing," Nature **629**, 784–790 (2024).
17. D. Zhu, L. Shao, M. Yu, *et al.*, "Integrated photonics on thin-film lithium niobate," Adv. Opt. Photonics **13**, 242–352 (2021).
18. Y. Qi and Y. Li, "Integrated lithium niobate photonics," Nanophotonics **9**, 1287–1320 (2020).
19. A. Honardoost, K. Abdelsalam, and S. Fathpour, "Rejuvenating a versatile photonic material: thin-film lithium niobate," Laser Photonics Rev. **14**, 2000088 (2020).
20. R. Weis and T. Gaylord, "Lithium niobate: summary of physical properties and crystal structure," Appl. Phys. A **37**, 191–203 (1985).
21. M. Dayarathna, Y. Wen, and R. Fan, "Data center energy consumption modeling: a survey," IEEE Commun. Surv. Tutor. **18**, 732–794 (2015).
22. Y. Hu, D. Zhu, S. Lu, *et al.*, "Integrated electro-optics on thin-film lithium niobate," Nat. Rev. Phys. **7**, 237–254 (2025).
23. M. He, M. Xu, Y. Ren, *et al.*, "High-performance hybrid silicon and lithium niobate Mach–Zehnder modulators for 100 Gbit s^{-1} and beyond," Nat. Photonics **13**, 359–364 (2019).
24. P. Kharel, C. Reimer, K. Luke, *et al.*, "Breaking voltage–bandwidth limits in integrated lithium niobate modulators using micro-structured electrodes," Optica **8**, 357–363 (2021).
25. X. Zhu, M. M. de Freitas, S. Shi, *et al.*, "Ultra wideband dual-output thin film lithium niobate intensity modulator," IEEE J. Sel. Top. Quantum Electron. **30**, 9200113 (2024).
26. X. Zhu, M. M. De Freitas, S. Shi, *et al.*, "Folded sub-1 V V_π thin film lithium niobate phase modulator," IEEE Photonics Technol. Lett. **37**, 301–304 (2025).
27. M. Yu, D. Barton, III, R. Cheng, *et al.*, "Integrated femtosecond pulse generator on thin-film lithium niobate," Nature **612**, 252–258 (2022).
28. Y. Song, Y. Hu, X. Zhu, *et al.*, "Integrated electro-optic digital-to-analogue link for efficient computing and arbitrary waveform generation," Nat. Photonics **19**, 1107–1115 (2025).
29. H. Feng, T. Ge, X. Guo, *et al.*, "Integrated lithium niobate microwave photonic processing engine," Nature **627**, 80–87 (2024).
30. Y. Gao, V. Torres-Company, and J. Schröder, "Suppressed plasmonic mode coupling for efficient electro-optic lithium niobate modulator," Opt. Express **33**, 37784–37794 (2025).
31. X. Meng, C. Yuan, X. Cheng, *et al.*, "Thin-film lithium niobate modulators with ultra-high modulation efficiency," Laser Photonics Rev. **19**, 2400809 (2025).
32. N. Chen, K. Lou, Y. Yu, *et al.*, "High-efficiency electro-optic modulator on thin-film lithium niobate with high-permittivity cladding," Laser Photonics Rev. **17**, 2200927 (2023).

33. C. Li, J. He, M. Zhang, *et al.*, "Ultra-low-loss slow-light thin-film lithium niobate optical modulator," Laser Photonics Rev. **19**, e01998 (2025).
34. J. Shen, Y. Zhang, L. Zhang, *et al.*, "Highly efficient slow-light Mach–Zehnder modulator achieving 0.21 V cm efficiency with bandwidth surpassing 110 GHz," Laser Photonics Rev. **19**, 2401092 (2025).
35. L. Chen, Q. Xu, M. G. Wood, *et al.*, "Hybrid silicon and lithium niobate electro-optical ring modulator," Optica **1**, 112–118 (2014).
36. M. Li, J. Ling, Y. He, *et al.*, "Lithium niobate photonic-crystal electro-optic modulator," Nat. Commun. **11**, 4123 (2020).
37. R. Krähenbühl and M. Howerton, "Investigations on short-path-length high-speed optical modulators in $LiNbO_3$ with resonant-type electrodes," J. Light. Technol. **19**, 1287–1297 (2001).
38. T. Kawanishi, S. Oikawa, K. Higuma, *et al.*, "Design of $LiNbO_3$ optical modulator with an asymmetric resonant structure," IEICE Trans. Electron. **85**, 150–155 (2002).
39. J. Zhang, C. Wang, C. Denney, *et al.*, "Ultrabroadband integrated electro-optic frequency comb in lithium tantalate," Nature **637**, 1096–1103 (2025).
40. J. Shin, C. Ozturk, S. Sakamoto, *et al.*, "Novel T-rail electrodes for substrate removed low-voltage high-speed GaAs/AlGaAs electrooptic modulators," IEEE Trans. Microw. Theory Tech. **53**, 636–643 (2005).
41. Z. Wang, G. Chen, Z. Ruan, *et al.*, "Silicon–lithium niobate hybrid intensity and coherent modulators using a periodic capacitively loaded traveling-wave electrode," ACS Photonics **9**, 2668–2675 (2022).
42. D. M. Pozar, *Microwave Engineering: Theory and Techniques* (Wiley, 2021).
43. Y. Gao, F. Lei, M. Girardi, *et al.*, "Compact lithium niobate microring resonators in the ultrahigh Q/V regime," Opt. Lett. **48**, 3949–3952 (2023).
44. Y. Gao, Y. Sun, I. Rebolledo-Salgado, *et al.*, "Tightly-confined and long Z-cut lithium niobate waveguide with ultralow-loss," Laser Photonics Rev. **19**, e00042 (2025).
45. L. Alloatti, D. Korn, R. Palmer, *et al.*, "42.7 Gbit/s electro-optic modulator in silicon technology," Opt. Express **19**, 11841–11851 (2011).
46. W. Heni, C. Haffner, D. L. Elder, *et al.*, "Nonlinearities of organic electro-optic materials in nanoscale slots and implications for the optimum modulator design," Opt. Express **25**, 2627–2653 (2017).
47. Y. Gao, Y. Sun, P. Andreksonand, *et al.*, "Original data of "Ultra-compact and efficient standing-wave electro-optic modulator in lithium niobate"," Zenodo (2026), https://doi.org/10.5281/zenodo.20391751.